

Numerical Methods in Astrophysics

## Project 2

# Ordinary Differential Equations, Fourier Transforms and Spectral Analysis

*Saksham Kaushal*

## Contents

<b>1</b>	<b>Introduction</b>	<b>2</b>
<b>2</b>	<b>Part 1 - Ordinary Differential Equations</b>	<b>3</b>
2.1	Methods . . . . .	3
2.2	Results . . . . .	4
2.3	Discussions . . . . .	5
<b>3</b>	<b>Part 2 - Fourier Transform and Spectral Analysis</b>	<b>8</b>
3.1	Methods . . . . .	8
3.2	Results . . . . .	8
3.3	Discussions . . . . .	10
<b>4</b>	<b>Conclusions</b>	<b>11</b>
	<b>References</b>	<b>11</b>

# 1 Introduction

Ordinary differential equations with no analytical solutions can be integrated numerically to obtain their solutions in particular conditions. Runge-Kutta methods can be used for such numerical integration in initial value problems. Fourth order Runge-Kutta method is most often used and is accurate to fourth power in Taylor's expansion. This is defined as follows [1].

$$y_{n+1} = y_n + \frac{k_1}{6} + \frac{k_1}{6} + \frac{k_2}{3} + \frac{k_3}{3} + \frac{k_4}{6} + \mathcal{O}(h^5), \quad (1)$$

where,

$$\begin{aligned} k_1 &= hf(x_n, y_n), \\ k_2 &= hf\left(x_n + \frac{h}{2}, y_n + \frac{k_1}{2}\right), \\ k_3 &= hf\left(x_n + \frac{h}{2}, y_n + \frac{k_2}{2}\right), \\ k_4 &= hf(x_n + h, y_n + k_3). \end{aligned}$$

Here  $h$  is the step-size for integration and its value can be adjusted dynamically depending on the region of the function being integrated. Such a technique uses adaptive step-size by calculating  $n^{th}$  value of  $h$  as [2]

$$h_n = h_{n-1} \left| \frac{\Delta_0}{\Delta} \right|^m, \quad (2)$$

where  $h_n$  is the new updated step-size,  $h_{n-1}$  is the previous step-size and  $m$  is an exponent usually in the range  $[0.2, 0.25]$ , optionally set to different values when increasing or decreasing the step-size.

A physical process can be represented in either time-domain or frequency domain [1], according to the relations [4],

$$H(\omega) = \int_{-\infty}^{\infty} e^{i\omega t} h(t) dt, \quad (3)$$

$$h(t) = \frac{1}{2\pi} \int_{-\infty}^{\infty} e^{-i\omega t} H(\omega) d\omega. \quad (4)$$

We can go from time-domain representation of a function to frequency domain representation and vice-versa using Fourier transforms and inverse Fourier transform, respectively. An optimized method for calculating discrete Fourier transform employs an algorithm of time complexity at least  $\mathcal{O}(N \log_2 N)$  as opposed to  $\mathcal{O}(N^2)$  in normal case. This method is known as fast Fourier transform. By calculating power spectrum of a function using Fourier transform, an analysis of different constituent frequencies can be performed. For a real-valued  $h(t)$ , power spectral density (PSD) can be calculated using the relation below [4]. This estimator of power is known as periodogram.

$$P_h(\omega_n) = \frac{2}{N^2} |H_n|^2. \quad (5)$$

This section introduced the basic principles of numerical methods involved in this study. In sections 2 and 3 the methods, results and discussion of observations are presented for part 1 and 2 of the project respectively. Section 4 gives a brief summary of physical phenomena studied using these simulations along with conclusions derived from both parts of the project.

## 2 Part 1 - Ordinary Differential Equations

For stars in disk of the galaxy, equation of motion is given by equation 19 of [2] as,

$$\frac{d^2r(t)}{dt^2} = -\nabla\Phi(r) - 2\Omega_B \times v + \Omega_B^2 r, \quad (6)$$

where  $\Omega_B$  is angular velocity and the gravitational potential,  $\Phi(r)$  in the two dimensions for an elongated bar structure is given by equation 20 of [2] as,

$$\Phi(x, y) = \frac{v_0^2}{2} \ln(a^2 + x^2 + \frac{y^2}{q^2}). \quad (7)$$

The gradients of gravitational potential along the two axes are given by partial derivatives of equation (7) with respect to  $x$  and  $y$  as follows,

$$\frac{\partial\Phi}{\partial x} = \frac{v_0^2 x}{a^2 + x^2 + \frac{y^2}{q^2}}, \quad (8)$$

$$\frac{\partial\Phi}{\partial y} = \frac{v_0^2 y}{q^2(a^2 + x^2 + \frac{y^2}{q^2})}. \quad (9)$$

We can substitute equations (8) and (9) in equation (6) to obtain the equation of motion that can be solved in our simulation. Equations along the two axes are given by,

$$a_x = \frac{d^2x}{dt^2} = -\frac{v_0^2 x}{a^2 + x^2 + \frac{y^2}{q^2}} + 2\Omega_B v_y + x\Omega_B^2, \quad (10)$$

$$a_y = \frac{d^2y}{dt^2} = -\frac{v_0^2 y}{q^2(a^2 + x^2 + \frac{y^2}{q^2})} - 2\Omega_B v_x + y\Omega_B^2, \quad (11)$$

where it must be noted that for second term on the right hand side of equation (10), the cross product  $\Omega_B \times v_x = -v_y$  and for similar term in equation (11),  $\Omega_B \times v_y = v_x$ , where  $\Omega_B$  has the direction perpendicularly outwards from the x-y plane.

The value of *Jacobi integral* is conserved as a star moves in a rotating barred potential and therefore, minimum dispersion in its values throughout the simulation indicates better numerical integration. Its value is given by

$$E_j \equiv \frac{\dot{r}^2}{2} + \Phi - \frac{(\Omega_B \times r)^2}{2}. \quad (12)$$

From equation 13 of [2], the numerical error in each integration time-step can be controlled by adapting the step-size according to the maximum permissible error. If we define,

$$\Delta_0 \equiv \epsilon y_{max}, \quad (13)$$

then  $\Delta < \Delta_0$  should be satisfied for each integration step, where  $\Delta$  is the numerical error of a given step,  $\epsilon$  is the parameter defining the accuracy of integration and  $y_{max}$  is the amplitude of function in the range over which function is being integrated. If this inequality does not hold true, the values need to be adjusted accordingly, and the integration step is repeated with reduced step-size until this inequality is satisfied. However, if this inequality does indeed hold true such that  $\Delta \ll \Delta_0$ , integration step-size can be safely increased to reduce the difference between  $\Delta$  and  $\Delta_0$ . The step-size can be update according to equation 2.

### 2.1 Methods

In the FORTRAN code *orbit19.f*, the four elements of array *ys* represent the values of  $x$ ,  $v_x$ ,  $y$  and  $v_y$  respectively. Value of  $a$ ,  $q$ ,  $v_0$  and  $\Omega_B$  are represented by variables *a*, *q*, *v0* and *om*. The difference between the variables *x2* and *x1* indicates the time for which the simulation takes place. This is essentially different from time-step of the simulation, that depends on the value of  $\epsilon$ , which parameterizes the accuracy of integration. The four elements of array *dxdy* represent the values of  $v_x$ ,  $a_x$ ,  $v_y$  and  $a_y$ . The values of  $a_x$  and  $a_y$  are calculated using the equations (10) and (11), and encoded in the subroutine *derivs* in the code. The Jacobi integral, given by equation (12) is assigned the variable *ej*.

The following methods were employed for different tasks performed for this part of the project:

Parameter	Variable	Value
$\Omega_B$ (Angular velocity)	om	1.0
$v_0$	v0	1.0
$a$	a	0.03
$q$	q	0.8
$t_1$ (Initial time)	x1	0.0
$t_2$ (Final time)	x2	5.0
$x$	ys(1)	0.0
$v_x$	ys(2)	-1.68
$y$	ys(3)	0.087
$v_y$	ys(4)	0.0

**Table 1:** Initial parameters of the simulation, variable names assigned to them in the FORTRAN code and their initial values set for the first simulation.

1. The missing  $x$  and  $y$  components of the equation of motion for a star in barred potential well are encoded in the subroutine `derivs` of FORTRAN program `orbit19.f` as,

$$\begin{aligned} dydx(2) &= -y(1)*v0**2/(a**2+y(1)**2+(y(3)**2/q**2))+2*om*y(4)+y(1)*om**2, \text{ and} \\ dydx(4) &= -y(3)*v0**2/(q**2*(a**2+y(1)**2)+y(3)**2)-2*om*y(2)+y(3)*om**2 . \end{aligned}$$

These are the  $a_x$  and  $a_y$  components, given by equations (10) and (11). The  $v_x$  and  $v_y$  components were already assigned to array elements `dxdy(1)` and `dxdy(3)` respectively.

2. Initial parameters of the simulation for this task, along with their values and variable names in the program are mentioned in Table 1.
3. The value of  $\epsilon$  varies the number of time-steps involved, and therefore controls the accuracy of integration. For the initial conditions given in Table 1, simulation is run for values of  $\epsilon$  equal to  $10^{-5}, 10^{-6}, 10^{-7}, 10^{-8}$  and  $10^{-9}$ . The value of Jacobi integral, defined above, is inspected for each of these values of  $\epsilon$  and plotted on a graph using Python and its associated libraries like numpy, pandas, matplotlib and seaborn. All subsequent plotting is performed in a similar manner.
4. The value of variable `x2`, defining the final time of simulation, is changed from initial value of 5.0 to a new value of 20.0, keeping all other parameters unaltered. The trajectories calculated in both the cases are then plotted.
5. The value of  $v_x$  assigned to array element `ys(2)` is changed to values -1.64, -1.635, -1.63, -1.58, -1.15, -0.6, -0.524 and -0.4, and the simulation is run for each of these values to obtain the corresponding trajectories which are plotted for a final time of 20.0.

## 2.2 Results

- For different values of  $\epsilon$ , the variations in values of Jacobi integral are plotted in figure 1 upto a final time of 5.0. The variations are most prominent for highest and lowest values of  $\epsilon$ , and least for intermediate values. Analytically, the Jacobi integral is a conserved quantity for a three-body problem in a non-inertial frame of reference. Therefore, minimum variation in its value corresponds to most accurate numerical integration, which eventually gives us the most suitable value of  $\epsilon$ .

From the graph in figure 1 and using the values of standard deviations for different values of  $\epsilon$  from table 2, we can conclude that  $\epsilon = 10^{-7}$  is the most suitable value for integration.

- The trajectories for a star with initial parameters defined in section 2.1, for final times of 5.0 and 20.0 in simulation are plotted in figure 2.
- The calculated trajectories for a final time of 20.0 corresponding to initial values of  $v_x = -1.68, -1.64$  and  $-1.635$  are plotted for comparison in figure 3-(Top). The individual trajectories are plotted separately in figures 2(b) and 3-(Bottom).
- Similar plots for initial values of  $v_x = -1.63, -1.58, -1.15, -0.6, -0.524$  and  $-0.4$  are plotted for comparison in figure 4-(Top) and separately in figure 4-(Bottom).

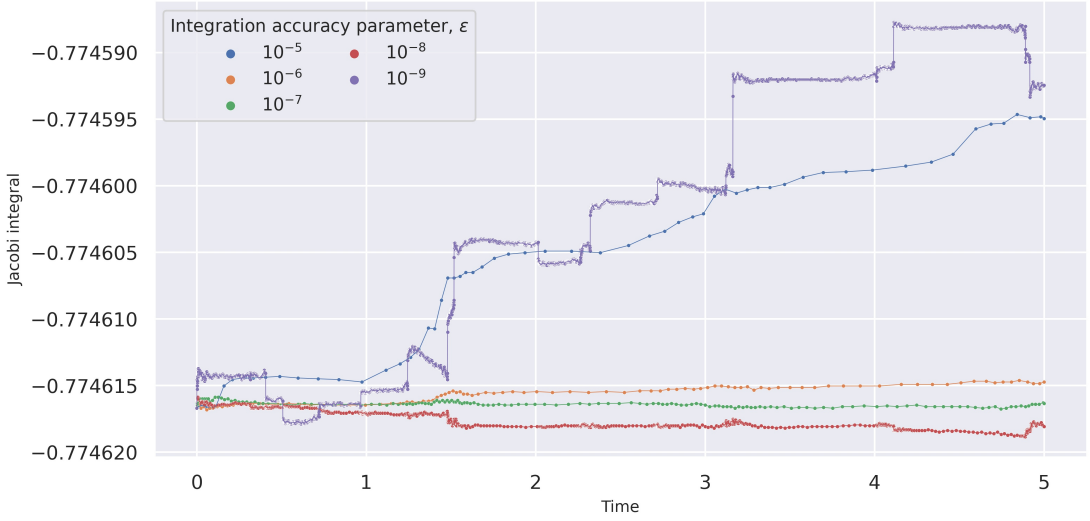


**Figure 1:** Variation of Jacobi integral with time for different values of  $\epsilon$ , a parameter that signifies the accuracy of integration.

$\epsilon$	$\sigma_{E_j}$
$10^{-5}$	$7.326 \times 10^{-6}$
$10^{-6}$	$6.490 \times 10^{-7}$
$10^{-7}$	$1.887 \times 10^{-7}$
$10^{-8}$	$6.918 \times 10^{-7}$
$10^{-9}$	$1.013 \times 10^{-5}$

**Table 2:** Standard deviation ( $\sigma_{E_j}$ ) in values of Jacobi Integral for different values of integration accuracy parameter ( $\epsilon$ ).

### 2.3 Discussions

1. The accuracy of integration increases with reduction in time-step, although it increases execution time. However, below a certain value of integration accuracy parameter,  $\epsilon$ , the accuracy tends to decrease, as seen in figure 1.
2. The trajectory followed by the star with  $v_x = -1.635$  in figure 3(b) is a case of *stable periodic orbit* [3]. Such an orbit has a closed geometry and the motion repeats after a fixed interval of time.
3. Slight variation in the parameters from the case of  $v_x = -1.635$ , we get *trapped orbits* [3]. Examples of such orbits are for  $v_x = -1.64$  and  $-1.68$ . A larger deviation in parameters from the stable periodic orbit leads to a less tightly bound trapped orbit, as in the case of  $v_x = -1.68$ . Such orbits are neither periodic nor closed and tend to stay in the vicinity of the parent stable periodic orbit.
4. Similar trend can be noted in figure 4, where the stable periodic orbit occurs at  $v_x = -0.524$  (figure 4(e)). A morphological transition in orbits can be seen as we move from one stable periodic orbit ( $v_x = -1.635$ ) to another ( $v_x = -0.524$ ). Accordingly, the orbit for  $v_x = -1.15$ , for which the initial parameters deviate the most, from the two periodic stable orbits, ends up being the trapped orbit with most loosely bound morphology.
5. With decrease in  $v_x$ , we get orbits that are more tightly bound to the center of the potential well. This trend can be seen through the decreasing span of orbits along x-axis as we move to lower values of  $v_x$  in figures 3 and 4.

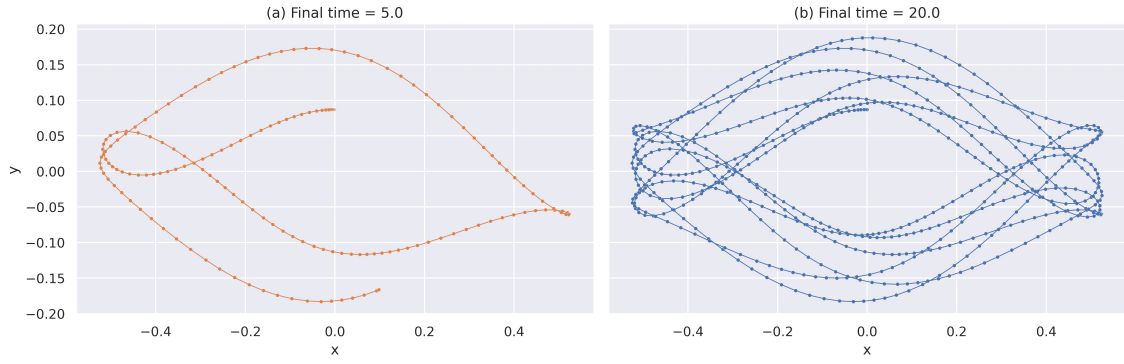


**Figure 2:** Trajectories followed over (a) 5.0 units and (b) 20 units of time by a star with initial parameters,  $(x, y) = (0, 0.087)$  and  $(v_x, v_y) = (-1.68, 0)$ .

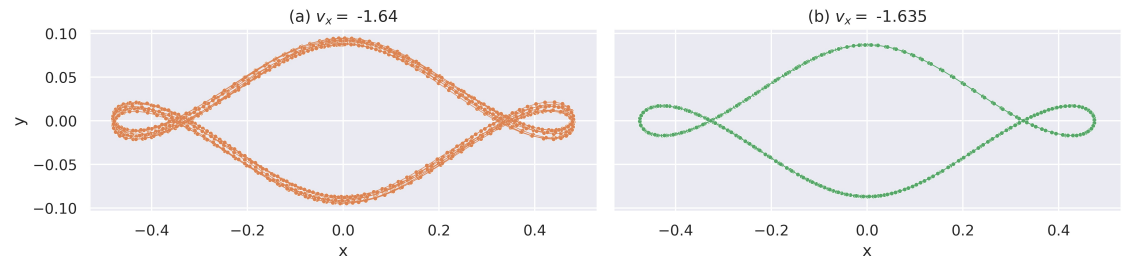
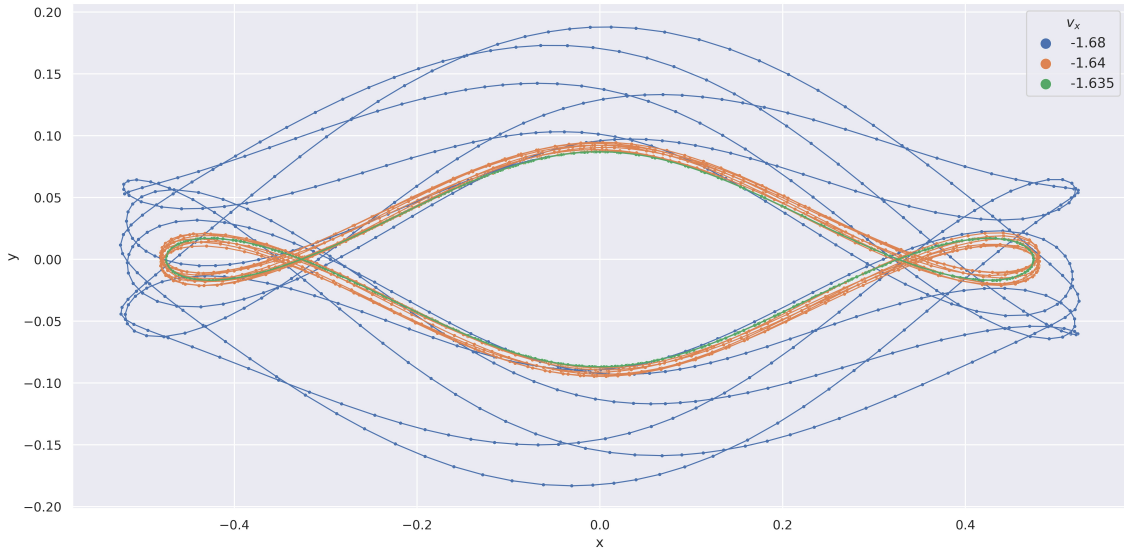


**Figure 3:** (Top) A comparison plot showing trajectories followed by a star for different initial values of  $v_x$ . (Bottom 1  $\times$  2 grid) Trajectories followed by a star for initial values of  $v_x$  equal to (a) -1.64, and (b) -1.635 shown separately. Note that the trajectory for  $v_x = -1.68$  is shown individually in figure 2(b).

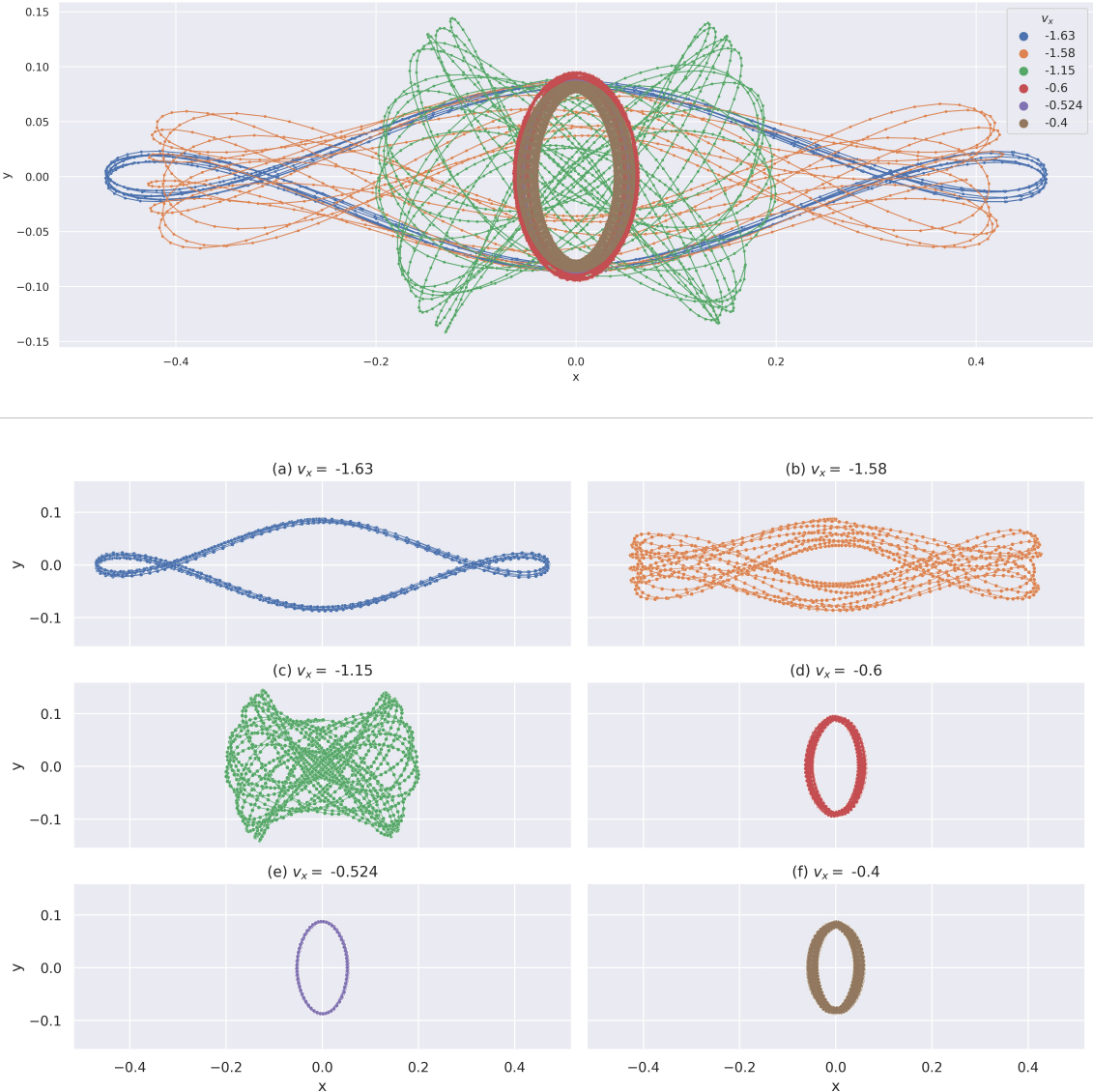


**Figure 4:** (Top) A comparison plot showing trajectories followed by a star for different initial values of  $v_x$ . (Bottom  $3 \times 2$  grid) Trajectories followed by a star for initial values of  $v_x$  equal to (a)  $-1.63$ , (b)  $-1.58$ , (c)  $-1.15$ , (d)  $-0.6$ , (e)  $-0.524$  and (f)  $-0.4$  shown separately.

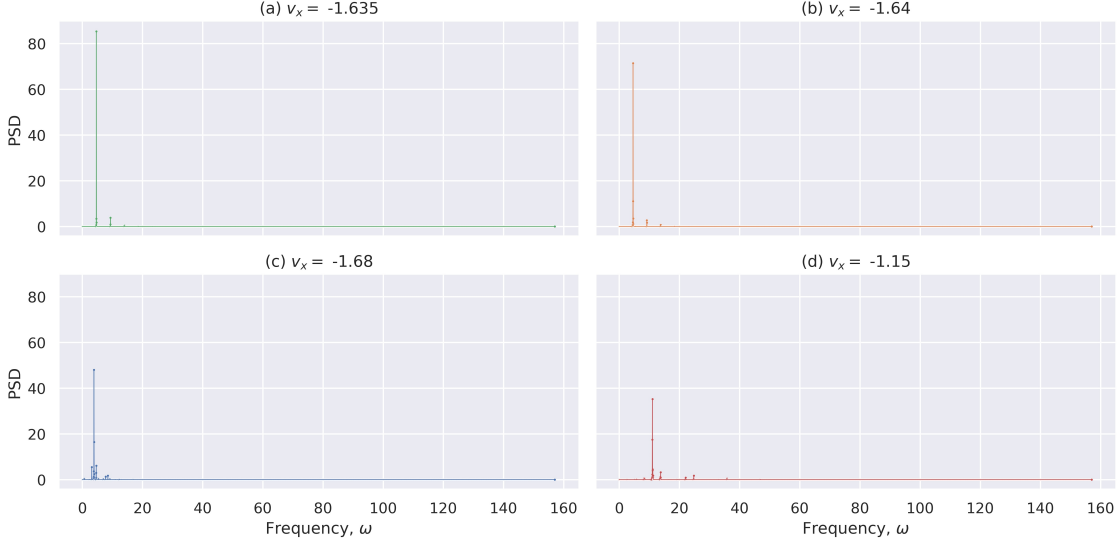


**Figure 5:** One-sided power spectral density (in %) vs frequency plots for various initial values of  $v_x$ .

### 3 Part 2 - Fourier Transform and Spectral Analysis

The basic principles of Fourier transform and spectral analysis were discussed in section 1. For the highest frequency in the data to be resolved, it is necessary that a discrete Fourier transform is sampled above a critical sampling frequency known as Nyquist frequency, given by [4],

$$\omega_c = \frac{\pi}{\Delta}, \quad (14)$$

where,  $\Delta$  is the sampling interval. The value of  $\Delta$  for sampling any discrete Fourier transform needs to be optimized for obtaining correct results. An extremely small value of it increases critical sampling value and therefore, leads to power in frequencies below Nyquist frequency adding up and getting assigned to zero frequency. On the other hand, a large value of it would lead to aliasing, in which power at high frequencies gets *folded* and eventually added to low frequencies, essentially giving us incorrect results.

#### 3.1 Methods

In the FORTRAN code *fourier19.f*, the setup for the simulation is performed in a manner similar to that in section 2.1, with  $v_x = -1.635$ . The simulation produces output files containing values of the frequency running number ( $k$ ), the power spectral density as percentage ( $prw$ ) and the logarithm of this value ( $\log prw$ ). The value of  $k$  can be converted to frequency,  $\omega$  using the relation,

$$\omega = \frac{2\pi(k-1)}{KMAXX * step}, \quad (15)$$

where  $KMAXX = 2^{13} = 8192$  and  $step = 0.02$  are predefined in the program.

The value of  $v_x$ , assigned to variable `ys(2)`, is set to  $-1.635$ ,  $-1.64$ ,  $-1.68$  and  $-1.15$  in separate runs of the simulation, each producing a different output file to be analyzed.

#### 3.2 Results

- One-sided PSD for  $v_x = -1.635$  is plotted on linear scale in figure 5(a) and on logarithmic scale in figure 6(a). The initial few major peaks are listed in table 3a.
- One-sided PSD for  $v_x = -1.64$  is plotted on linear scale in figure 5(b) and on logarithmic scale in figure 6(b). The initial few major peaks are listed in table 3b.

<b>k</b>	<b><math>\omega</math></b>		<b>k</b>	<b><math>\omega</math></b>	
123	4.678	<i>a</i>	98	3.72	<i>b</i>
245	9.357	$\approx 2a$	121	4.602	<i>a</i>
367	14.036	$\approx 3a$	144	5.484	$\approx 2a - b$
488	18.676	$\approx 4a$	218	8.322	$\approx a + b$
610	23.355	$\approx 5a$	240	9.165	$\approx 2a$
732	28.03	$\approx 6a$	264	10.086	$\approx 3a - b$
854	32.71	$\approx 7a$	337	12.885	$\approx 2a + b$
...			360	13.767	$\approx 3a$
(a) $v_x = -1.635$ .			383	14.65	$\approx 4a - b$
			457	17.526	$\approx 3a + b$
			480	18.37	$\approx 4a$
			503	19.29	$\approx 5a - b$
...			...		...
					(b) $v_x = -1.64$ .
					(c) $v_x = -1.68$ . The starred rows comprise of peaks with a component $> 0.1\%$ of total power.

**Table 3:** Frequency running number ( $k$ ) and corresponding frequency values ( $\omega$ ) for few initial peaks in the data for different initial values of  $v_x$ . Algebraic representation of accompanying dependent frequencies in terms of independent frequencies is also given in the unlabeled rightmost column.

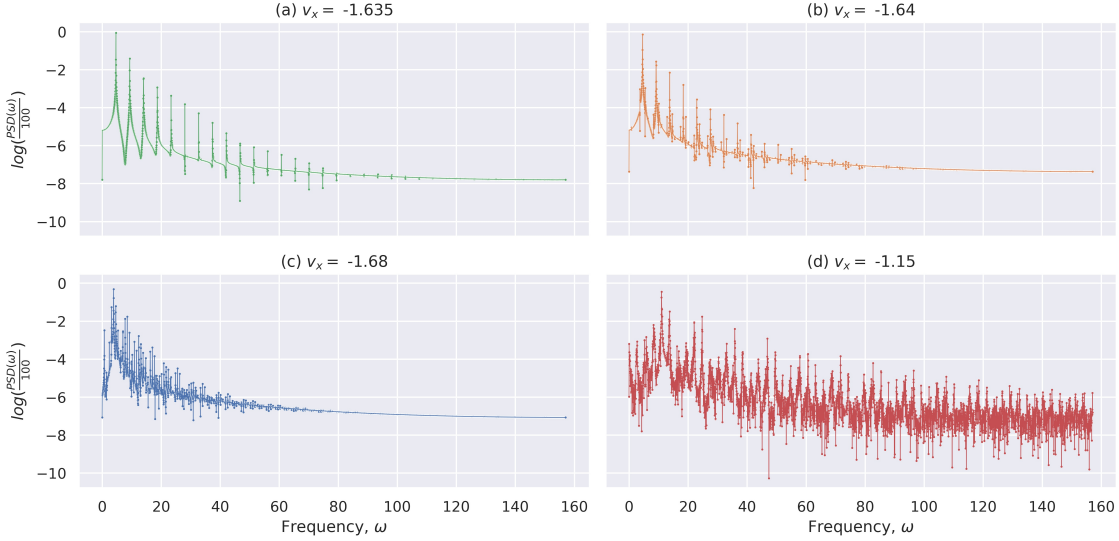


**Figure 6:** Logarithm (base 10) of one-sided power spectral density vs frequency plots for various initial values of  $v_x$ .

<b>k</b>	<b><math>\omega</math></b>	<b>% of total power</b>
289	11.045	35.177
360	13.767	3.23
647	24.77	1.73
356	13.61	1.214

**Table 4:** Frequencies and contribution to total power of major peaks in power spectrum for  $v_x = -1.15$ .

- One-sided PSD for  $v_x = -1.68$  is plotted on linear scale in figure 5(c) and on logarithmic scale in figure 6(c). The initial few major peaks are listed in table 3c.
- One-sided PSD for  $v_x = -1.15$  is plotted on linear scale in figure 5(d) and on logarithmic scale in figure 6(d). The frequencies of major peaks along with the values of how much percentage of total power they constitute are given in table 4.

### 3.3 Discussions

1. (a) Given that there is almost no power present in high frequencies, no significant aliasing is expected in this case.  
(b) There is no power at zero frequency and all power peaks lie at frequencies significantly higher than Nyquist frequency ( $= \frac{2\pi}{N\Delta}$ , from equation 14, where  $N = \text{KMAXX}$  and  $\Delta = \text{step}$  in the code). This indicates that unresolved peaks in power at low frequencies are not expected.  
(c) As can be seen from figure 6(a), the distribution of power spectral density consists of a set of sharp peaks.  
(d) From figure 6(a), it can be observed that the peaks do not occur randomly and their distribution across the range of frequencies seems regular. This can be confirmed from table 3a, where we see that these peaks occur at regular intervals of a frequency.
2. Table 3a enlists the frequencies at which peaks in power occur. Relations of these peaks to the primary peak are given in the last column, from which we can infer that peaks occur at frequencies which are integral multiples of frequency of the primary peak. No secondary peak is required to explain any peak in the sequence. Also, from the data, it is observed that the power in these peaks decreases with increase in the integral coefficient, in accordance with the property of Fourier transforms given in [4]. The frequency,  $\omega$  of the primary peak is 4.678 ( $k = 123$ ). Therefore all subsequent peaks can be represented as,  $\omega_n = 4.678n$ , where  $n = 2, 3, 4, \dots$ . Hence the trajectory oscillates with a single frequency,  $\omega = 4.678$ .

From section 2.3, we know that in this case, the star is in a stable periodic orbit. From preceding discussion we also know that this trajectory oscillates with a single frequency. Thus, we expect the star to be at the same point after each complete period of oscillation. Hence, after one period of oscillation, the star is located at the same point from where it started. This is confirmed by finding the coordinates of star after  $t = \frac{2\pi}{\omega}$ . Given  $\omega = 4.678$ , we get  $t \approx 1.343$ . By interpolation of data obtained in section 2.2 for  $v_x = -1.625$ , we obtain  $(x, y) = -0.0021, -0.0870$  at  $t = 1.343$ . For comparison,  $(x, y) = (0.0000, 0.870)$  at  $t = 0$  almost coincides with this value. Therefore, the star is observed at same location after one period.

3. (a) Similar to result 1 above, no significant aliasing or unresolved peaks at low frequencies are expected in this case also, for reasons mentioned in part 1(a) and 1(b) respectively.  
(b) There exists some pattern in frequencies of the power peaks, however, as seen from table 3b, the pattern is much more complicated than for peaks in table 3a. As such, the pattern cannot be explained using a single frequency.  
(c) From the last column in table 3b, we can see that all major peaks can be explained using additional peaks due two main frequencies, i.e. 4.602 ( $k = 121$ ) and 3.72 ( $k = 98$ ).  
(d) The power in these two frequencies is  $\approx 71.384\%$  and  $\approx 0.093\%$  of total power respectively. However, some of the power of these peaks is distributed in nearby frequencies also.
4. (a) For figure 6(c), there exist several well-defined peaks, but the pattern in those peaks is almost incomprehensible. The number of those peaks is also much larger than in case of figure 6(b). As a consequence, percentage contribution of these peaks towards total power is also less in this case.  
(b) Each peak containing more than 0.1% of total power is marked with an asterisk in table 3c. All these peaks can be explained using a linear combination of two major peaks at frequencies 3.873 and 0.73, as can be seen from last column of table 3c.  
(c) These two independent frequencies contain  $\approx 48.022\%$  and  $\approx 0.325\%$  of total power.

## 4 Conclusions

In this project we study the orbits of objects in barred potential wells, which represent the physical scenario of stars in the bars of the galaxies. The trajectories vary substantially as we alter parameters like initial position and velocity. On the quantitative analysis side of our study, how precisely we calculate these trajectories has a profound impact on our observations and understandings.

The ordinary differential equations can be numerically integrated using several methods. In this project, equation of motion of star in a potential was integrated using fourth order Runge-Kutta method. The accuracy and precision of our integration was tested by analyzing the values of a quantity conserved over time, known as the Jacobi integral. Orbits for various combinations of parameters were obtained and their morphology was examined.

A subset of these orbits was then analyzed using Fourier transforms. From power spectrum analysis of these orbits, we obtained the distribution of power in orbits across a range of frequencies.

We conclude that stable periodic orbits oscillate at a single frequency and therefore a star in such an orbit is expected to undergo periodic motion over a closed trajectory. On the other hand, trapped orbits oscillate at a combination of multiple frequencies. A star in such an orbit tends to remain in vicinity of its parent stable periodic orbit and follows a trajectory with open geometry. The more the initial parameters mentioned above vary for a star in trapped orbit, the lesser it tends to remain in vicinity of parent stable periodic orbit. Also, with decrease in velocity, a star follows an orbit that spans less farther away from the center of potential well.

## References

- [1] William H. Press et al. *Numerical Recipes in Fortran 77: The Art of Scientific Computing*. 2nd edition. Cambridge England ; New York: Cambridge University Press, Sept. 25, 1992. 933 pp. ISBN: 978-0-521-43064-7.
- [2] Witold Maciejewski. “Lecture 3: Notes on Ordinary Differential Equations”.
- [3] *Orbits in Realistic Galaxy Potentials - LAM - Laboratoire d’Astrophysique de Marseille*. URL: <https://www.lam.fr/anciennes-pages-d-equipe/dynamique-des-galaxies/dagal/dagal-lam/orbits-in-realistic-galaxy/?lang=fr>.
- [4] Witold Maciejewski. “Lecture 4: Notes on Fourier Transform and Spectral Analysis”.